Ruddlesden–Popper 2D Chiral Perovskite-Based Solar Cells

Adva Shpatz Dayan, Małgorzata Wierzbowska, and Lioz Etgar*

In this work, 2D chiral perovskite is demonstrated, where the barrier molecules are the two enantiomers (R)-(+)-α-Methylbenzylamine (R-MBA) and (S)-(-)-α-Methylbenzylamine (S-MBA). The chirality is manifested at high χ values and pure 2D structure measured by circular dichroism (CD) (where the perovskite general formula is ABX$_3$ χ (S/R-MBA)$_2$PbI$_4$, χ is the ratio of the barrier molecule to the small cation (A$^+$)). The anisotropy factor (g_{abs}) decreased by an order of magnitude when decreasing the χ value achieving 0.0062 for pure 2D. Ab initio many-body perturbation theory successfully describes the bandgaps, absorbance, and CD measurements. For the first time, these quasi-2D chiral perovskites are integrated into the solar cell. Using circular polarization (CP) and cutoff filter, the chirality effect from the solar cells photovoltaic response is able to be distinguished. It is revealed that at high χ values, the chirality affects the current density of the solar cell more than at low χ values while the open-circuit voltage didn't change. These chiral 2D perovskite are new class of materials which open the way for polarized hybrid perovskite.

1. Introduction

Organic–inorganic halide perovskite is considered as a promising material for solar cells (SCs) applications due to its suitable and excellent properties.[1,2] The special structure of organic and inorganic components within the same molecular composite enables control over the optical properties.[3–5] Organic–inorganic perovskite which is used in SCs usually is a semiconductor with direct bandgap (E_g), which can be tuned by changing the ratio of the cations and halides in the perovskite structure.[6–8] It has high absorption coefficient, long diffusion lengths and low exciton binding energy (E_b).[9–14] As a result of these superior properties, perovskite-based solar cells (PSCs) achieve power conversion efficiency (PCE) exceeding 25%.[15]

The perovskite's structure is ABX$_3$ where A is an organic/inorganic cation, B is a divalent metal ion (e.g., Cu^{2+}, Mn^{2+}, Sn^{2+}, and Pb^{2+}), and X is a halide (Cl$^-$, Br$^-$, or I$^-$).[16]

A. Shpatz Dayan, L. Etgar
Institute of Chemistry
Casali Center for Applied Chemistry
The Hebrew University of Jerusalem
Jerusalem 91904, Israel
E-mail: lioz.etgar@mail.huji.ac.il

M. Wierzbowska
Institute of High Pressure Physics
Polish Academy of Sciences
Sokołowska 29/37, 01-142 Warsaw, Poland

The ORCID identification number(s) for the author(s) of this article can be found under https://doi.org/10.1002/sstr.202200051.

The inorganic layers in the lattice consist of corner-sharing metal halide octahedra sheets (BX$_6$) where the organic A cation fits into the octahedral cage forming a 3D structure.[17–19] However, in the case of 2D perovskite, the [BX$_6$]$^{4-}$ octahedra are forming layers separated by large organic cations, which dedicated the number of the inorganic perovskite layers χ as presented in **Figure 1**. Based on the stoichiometry of the small organic ammonium cation and the large organic ammonium cation, it is possible to determine the number of perovskite's layers based on the formula (R-NH$_3$)$_2$A$_{n-1}$B$_n$X$_{3n+1}$.[20,21] A pure 2D structure defined as $n = 1$ is presented in Figure 1 involving just the large organic cation (i.e., (R-NH$_3$)$_2$BX$_{3n+1}$). Quasi-2D structure refers to the case when the long organic cation is present in the structure (i.e., (R-NH$_3$)$_2$A$_{n-1}$BX$_{3n+1}$), $n > 1$. There are several types of 2D perovskites, the most common ones are Ruddlesden–Popper (RP) and Dion–Jacobson (DJ). RP relates to the case where there are two barrier molecules between the inorganic sheets, therefore the hydrocarbon tails "R" extend into the space between the perovskite sheets, forming a Van der Waals gap.[22–24] In DJ, there is only one barrier molecule between the inorganic sheets, so the interaction is mainly hydrogen/ionic bonds with the halogens in the perovskite inorganic sheets.[25–28] The use of 2D and quasi-2D perovskite in optoelectronic devices showed promising photovoltaic (PV) results, where quasi-2D perovskite-based SCs achieved 24.6% efficiency using butylammonium iodide (BAI) as an additive (the structure is mainly 3D perovskite).[29] In contrast, when BAI was used at low n value ($n = 5$), a PCE of 18.04% was achieved.[30]

Chiral molecules exist in two forms that are mirror images of each other (i.e., enantiomers). Their chemical composition is identical and the only approach to distinguish between them is by their spatial geometry. Although their similarity their electrical, biological and optical properties can be different.[31,32] An interesting optical property of chiral molecules is the ability of the enantiomers to absorb circular polarized light (CPL) having different rotating electric filed vectors (E), which called right or left circular polarized light (RCP/LCP). This phenomenon, known as circular dichroism (CD), is related usually to amino acids, DNA, and peptides. Inorganic semiconductors having CD response are relatively uncommon.[33–37] In 2007, Moloney et al. were the first to report on inorganic semiconductors that contain organic chiral molecules such as quantum dots (QDs), so that the QDs exhibit CD response.[38]

In addition, using chiral molecules as organic cations in metal lead halide perovskite was demonstrated by Billing et al., they
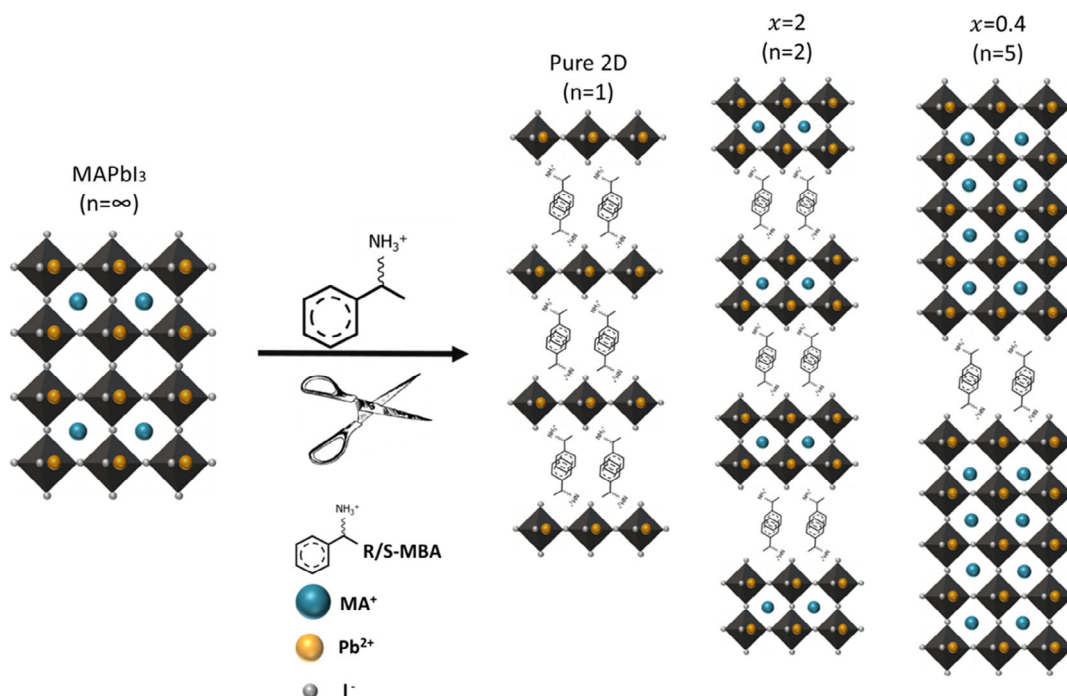
Figure 1. Schematic illustration of 2D, quasi 2D, and 3D structure using R/S-Methylbenzylamine (MBA) as the barrier molecules.

used the enantiomers (R)-(+)-α-Methylbenzylamine (R-MBA) and (S)-(-)-α-Methylbenzylamine (S-MBA).[39] Additional reports using chiral molecules in perovskite such as 1-(1-naphthyl)ethylamine and *sec*-butylamine were demonstrated studying their basic properties.[39–46] Most of the reports on chiral molecule in 2D structure are focused on pure 2D structure ($n = 1$), which can't function efficiently in the SC.[43,45]

In this work, we synthesize various 2D perovskites using chiral molecules having the general formula ABX_3 χ (S/R-MBA)$_2$PbI$_4$ where A is an organic/inorganic cation (in this work, MA$^+$ or combination of Cs$^+$ and FA$^+$), B is a divalent metal ion (in this work, Pb^{+2}), and X is a halide (in this work, I$^-$ or combination of I$^-$ and Br$^-$). (S/R-MBA)$_2$PbI$_4$ is pure 2D structure. χ is the ratio of the barrier molecules to the small cation (A$^+$) as presented in Figure 1. χ can be in the range of $0 < \chi \leq 2$. The highest χ value can be 2 where the general formula is (R/S-MBA)$_2$AB$_2$X$_7$. When $\chi = 0$, the material is 3D. We performed detailed optical characterizations (CD, photoluminescence [PL]), structural characterizations including powder X-Ray diffraction (pXRD), single-crystal XRD (SC-XRD), and morphological characterizations. Following that, we introduced these quasi-2D chiral perovskite into mesoporous PSCs studying the PV response, and supported it by the theoretical calculations.

2. Result and Discussion

Enantiomers are two stereoisomers which are mirror images of each other. In general, their properties are identical for example absorbance, PL, and other properties. When they present in a symmetric environment (e.g., using chiral solvent[47]), the enantiomers have identical chemical and physical properties except

for their ability to rotate plane-polarized light ($+/-$) by equal amounts but in opposite directions. **Figure 2**a,d presents the absorbance spectra of different χ values for pure 2D (R/S-MBA)$_2$PbI$_4$ ($\chi = 2$, 0.4, and 0.04) for both enantiomers S and R, respectively. It can be observed that the absorbance curves for the two enantiomers in the case of the same χ value are similar.

Usually, the absorbance spectra of 2D perovskite presents additional peaks that reflect the quantum confinement effect.[48] This effect changes the energy-level continuum in the bulk material into a discrete level structure which results in the enhancement of the oscillator strength of excitons through the increased spatial overlap between an electron and a hole. In our case, there is additional peak at ≈500 nm, which is related to $n = 1$. This peak can be observed in the case of pure 2D, $\chi = 2$, 0.4, and also at $\chi = 0.04$.

Figure 2b,e shows the PL for the various χ values of the two enantiomers. A redshift can be observed between the different χ values as expected in accordance with the absorbance. The PL lifetime of the S enantiomer for pure 2D and $\chi = 2$, 0.5, 0.15, and 3D can be observed in Figure 2c. The weighted average lifetime (τ show that pure 2D has the shortest lifetime of 1.2 ns, the lifetime increases to 3.5 ns for $\chi = 0.15$ while for the 3D structure it is the longest lifetime of 5.6 ns. This indicates that 3D perovskite has low rate of radiative recombination in comparison to the other low-dimensional perovskites as was further discussed by Even et al., which suggest that this might be related to the quantum confinement structure of the 2D perovskite.[49]

Moreover, the pronounced shifts of the main PL peaks with respect to the low-energy absorbance peaks suggest that the polaronic effects in these systems are strong. For example, calculating the difference between PL peak position to the
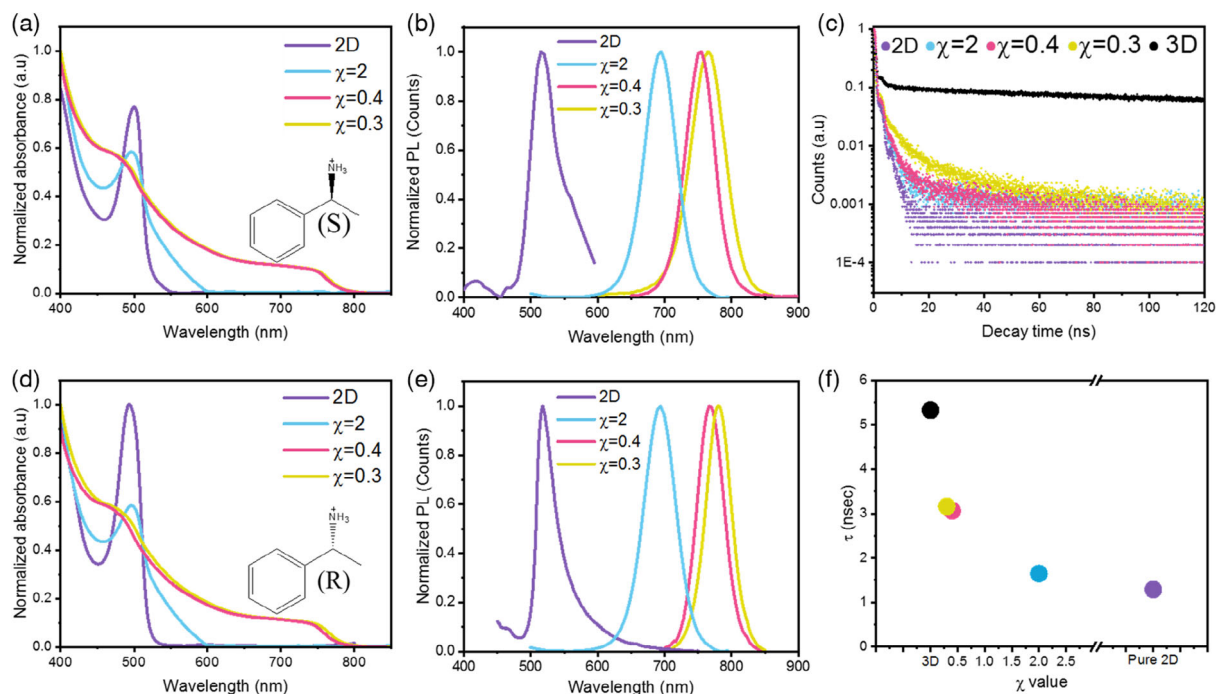
Figure 2. a) Absorbance spectra for MAPbBr$_{0.25}$I$_{0.75}$·χ (S-MBA)$_2$PbI$_4$, b) photoluminescence (PL) spectra for MAPbBr$_{0.25}$I$_{0.75}$· χ (S-MBA)$_2$PbI$_4$, c) PL decay for MAPbBr$_{0.25}$I$_{0.75}$ χ (S-MBA)$_2$PbI$_4$, and d) absorbance spectra for MAPbBr$_{0.25}$I$_{0.75}$· χ (R-MBA)$_2$PbI$_4$. e) PL spectra for MAPbBr$_{0.25}$I$_{0.75}$·χ (R-MBA)$_2$PbI$_4$. f) Calculated weighted average lifetime (τ) for MAPbBr$_{0.25}$I$_{0.75}$·χ (S-MBA)$_2$PbI$_4$.

absorbance peak position for the pure 2D results with an estimation of the exciton binding energy, 80 meV for the R-MBA and 100 meV for the S-MBA.

The bandgaps of the pure 2D were calculated by density-functional theory (DFT), and are 2.23 and 2.21 eV for (S-MBA)$_2$PbI$_4$ and (R-MBA)$_2$PbI$_4$, respectively, while the G$_0$W$_0$ corrections for the bandgaps are very small, 83 and 78 meV, yielding bandgap values of 2.31 and 2.29 eV, respectively. These values are in a good agreement with the experimental ones obtained from the absorbance spectrum of 520 nm (which is 2.38 eV). The emission spectra were also calculated and are presented in Figure S1, Supporting Information. For the calculations, we used the formalism of the Bethe–Salpeter equation (BSE), which includes the electron–hole pair interactions. The main optical dipole transitions take place from the iodide centered states to the lead localized states.

An essential characterization to recognize chiral materials is CD. This method involves circularly polarized light, that is, the differential absorption of left- and right-handed light.[50] When applying this analysis on non-chiral material, the CD spectra will be identical. However, when applying it on chiral materials, it is expected to observe a mirror spectra around $X = 0$.[50] **Figure 3** presents CD spectra for the various χ values, gray curve for S-MBA and blue for R-MBA. It can be seen that there is a reflection of the curve at $X = 0$. For pure 2D (Figure 3a), there are two peaks with opposite values; 496 and 510 nm. For $\chi = 2$ (Figure 3b), there is only one significant peak at 507 nm. For $\chi = 0.7$, there are similar peaks on 420 and 510 nm. All of those results indicate that the measured materials are chiral which react to polarized light. In contrast, in the case of $\chi = 0.4$

(Figure 3d), it is more difficult to see any significant peak around the X axis. Moreover, also in the case of higher n values ($\chi = 0.15$) (Figure S2, Supporting Information), there is no peak around the X axis. In these cases, there is no reflection curve; therefore, we conclude that the chirality is less significant in these cases. Usually, the CD for chiral molecule presents a curve that is on the same side of X axis for each enantiomer. In this case, the curve is under and above the X axis which represent the Cotton effect.[51] In this effect, the materials are different in their optical rotatory dispersion or circular CD which can be found near their E_g. This unique curve shape is related to splitting of the basic transition of the energy bands, which are excited by opposite circular polarization (CP).[52] The CD results indicate that the chiral barrier molecule influence the optical properties of the quasi-2D perovskite. This observation isn't trivial due to the complexity of the quasi-2D perovskite structure. Moreover, we calculated the CD spectra of the 2D perovskite and found a perfect agreement with the experimental results as can be seen in Figure 3e and S2, Supporting Information.

The anisotropy factor (g_{abs}) measures the strength of the CD signal at a given excitation intensity. This kind of calculation cancels the depended of CD on oscillator strength and concentration. The results are affected by overlapping transitions in the optical spectrum, which is why asymmetry assigned to each exciton state that can only be measured once the spectra are de-convoluted to different transitions.[53] Equation (1) shows the g_{abs} calculation[40,54] where A_L and A_R represent the intensity difference between right and left circularly polarized light on the samples, and the average absorbance intensity is $(1/2)(A_L + A_R)$. Ahn et al. reported that the anisotropy factor for pure 2D to be
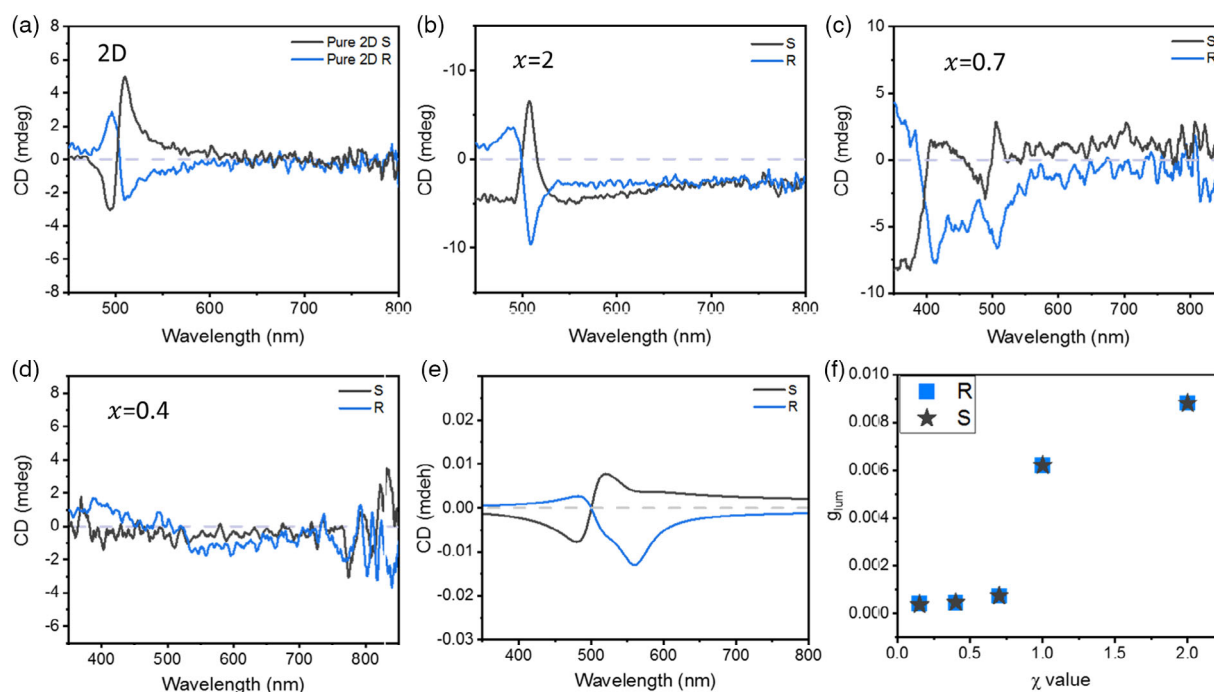
Figure 3. Circular dichroism (CD) spectra of both enantiomers a) pure 2D, b) $\chi = 2$, c) $\chi = 0.7$, and d) $\chi = 0.4$. e) The calculated CD spectra of pure 2D structures. f) Anisotropy factor as a function of χ.

6.3×10^{-3}.[46] In this work, we calculated the g_{abs} factor for the different χ values (Figure 3f); when the χ value increases, the g factor increases by order of magnitude.

$$g_{abs} = \frac{(A_L - A_R)}{0.5(A_L + A_R)} \tag{1}$$

To have a detailed crystallographic structure of our chiral 2D perovskite, we grew single crystals of pure 2D for S-MBA and R-MBA and performed SC-XRD and pXRD. Figure S3, Supporting Information, presents the structure of both pure 2D enantiomers measured by SC-XRD. The pXRD simulation of both enantiomers extracted from the SC-XRD can be seen at Figure S4, Supporting Information. It can be recognized that when we rotate the unit cell in the opposite angle, a reflection in the structure can be observed as expected from a chiral molecule (single-crystal CIF (crystallographic information file)). Growing well-defined single crystals of lower χ values is more complicated due to different diffusion coefficient and energetic preferences between the A cation (MA^+) and the barrier molecule (R/S-MBA). Therefore, we performed pXRD to explore the other χ values. **Figure 4** shows the perovskite pXRD patterns obtained from films with R-MBA (blue) and S-MBA (gray). In the case of pure 2D and $\chi = 2$ (Figure 4a–d), a 2D pXRD RP pattern can be observed. The XRD peaks are obtained at defined angles matching the 2D structure, including peaks at $2\theta < 10°$. However, for $\chi = 0.4$ (Figure 4e,f), in addition to the 2D structure, there are XRD peaks related to the 3D perovskite ($MAPbI_3$) at $2\theta = 14°$.

To verify the crystal structure of pure 2D for both enantiomers, we compared two kinds of films made by i) spin-coating

deposition of the exact stoichiometric ratio of the precursors and ii) dissolving a single crystal and redeposited it on the substrate. Both films were measured by pXRD (Figure S4, Supporting Information). It can be seen that for both enantiomers we observed the same peaks at the same angles, which support the fact that we obtained the desired composition using both methods.

Top-view scanning electron microscopy (SEM) images were taken for both enantiomers at the different χ values (pure 2D and $\chi = 0.4$, 0.3) (Figure S5, Supporting Information). The morphology is different for different χ values; however, the morphology between the enantiomers is very similar (comparing the same χ value). For example, pure 2D (Figure S5a,d, Supporting Information) shows needle-like structure for both enantiomers while in the case of $\chi = 0.3$ (Figure S5c,f, Supporting Information), the grains and the grain boundaries are relatively similar to the case of bulk perovskite.

Following the optical, physical, crystallographic, and theoretical calculations, we introduced the chiral quasi-2D perovskite into the PSCs to study its PV performance. PSCs having the two enantiomers with different χ values ($\chi = 0.3$, 0.2, 0.15) and $n = \infty$ (3D) were fabricated with the following structure FTO glass/mesoporous TiO_2/perovskite/Spiro-OMETAD/Au (inset of **Figure 5**d). To study the influence of the chiral molecules on the PV properties, we measured the PSCs with CP and cutoff filter. Two different lenses were used: the cutoff filter which limits the xenon lamp in range of 405–690 nm and the CP, which polarizes the wavelength, which goes through the cutoff filter in the range of 400–700 nm wavelength. We used two different lenses; the cutoff filter which delimited the xenon lamp in range of 405–690 nm and CP filter, which polarizes all the

ADVANCED
SCIENCE NEWS

www.advancedsciencenews.com

small
structures

www.small-structures.com
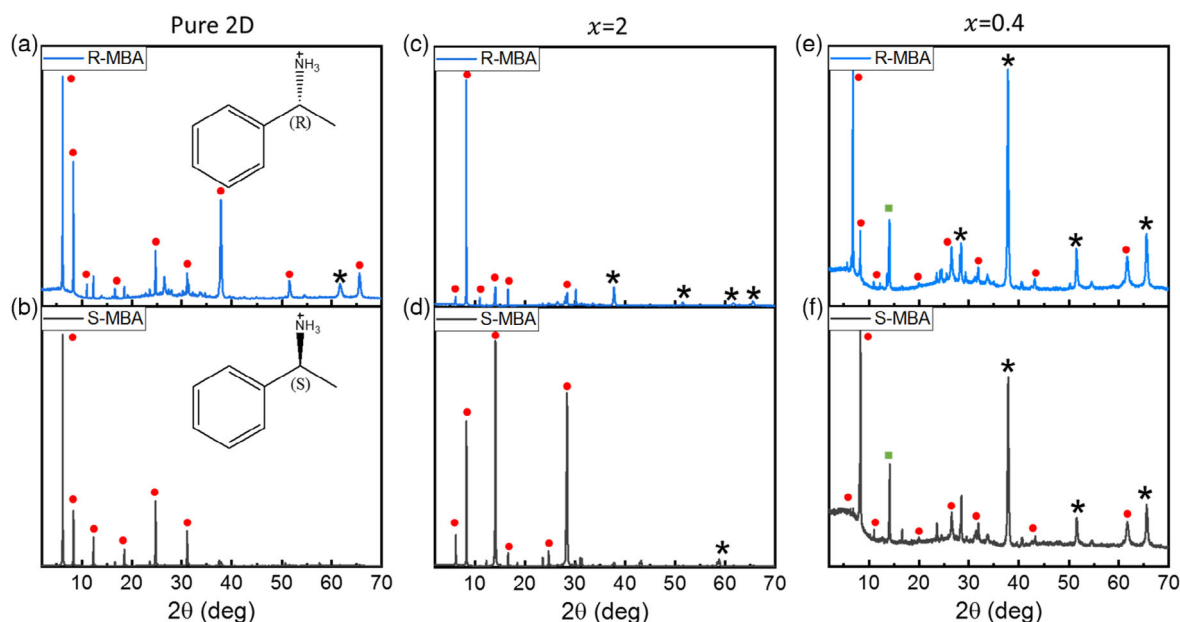
Figure 4. Powder X-Ray diffraction (pXRD) patterns for a,b) pure 2D, c,d) $\chi = 2$ (R/S-MBA)$_2$MAPb$_2$I$_7$, and e,f) $\chi = 0.4$ (R/S-MBA)$_2$MA$_4$Pb$_5$I$_{16}$, *—FTO, •—2D, ■—MAPbI$_3$.
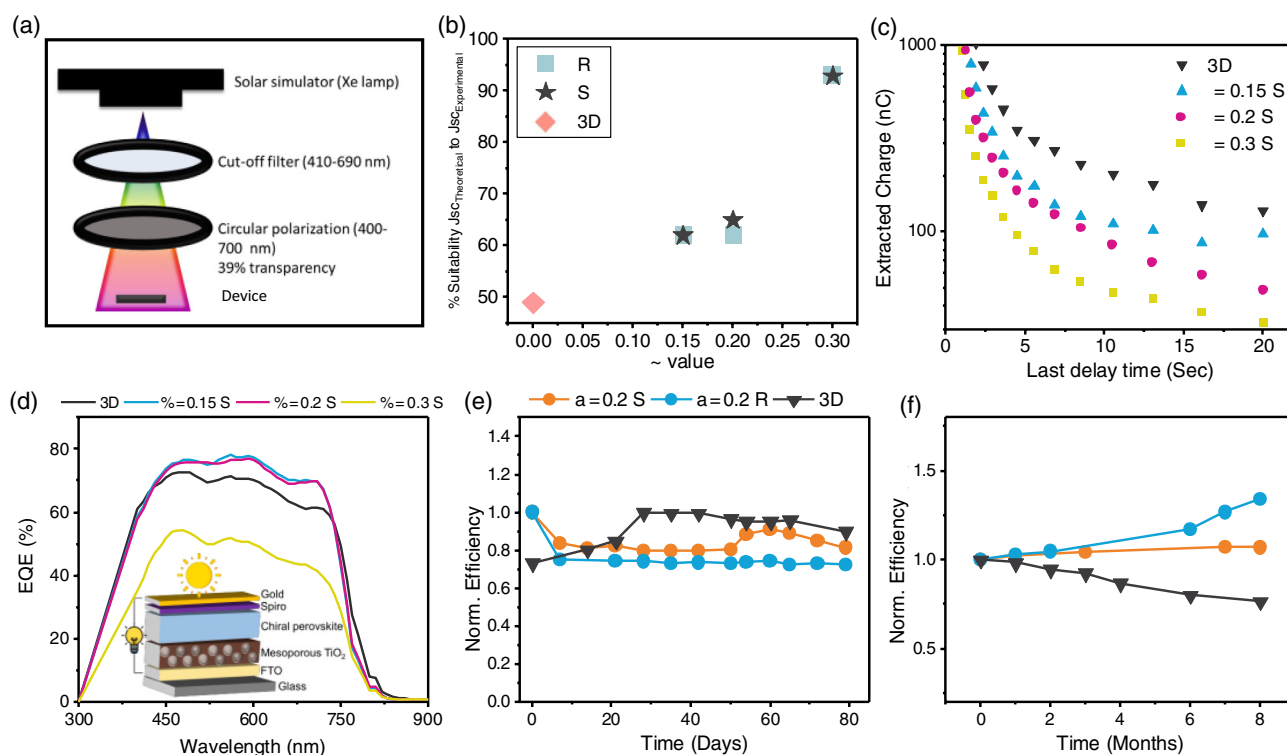
Figure 5. a) The setup measurement using cutoff filter and circular polarization. b) The suitability between the theoretic short-circuit current density (J_{SC}) to the experimental J_{SC}. % Sutability J_{SC} (theoretical) to Jsc (experimental) $= \frac{The\,J_{sc}\,that\,measured\,with\,only\,cut\,off\,filter \times 0.4}{The\,J_{sc}\,that\,measured\,with\,cut\,off\,filter\,and\,circular\,polarizer}$. c) Charge extraction (CE) measurements for 3D and $\chi = 0.15, 0.2, 0.3$ S enantiomer. d) External quantum efficiency (EQE) spectra for 3D and $\chi = 0.15, 0.2, 0.3$ S enantiomer. e) Stability measurements under ambient air for non-encapsulated devices with humidity of 43–49% for $\chi = 0.2$ for both enantiomers. f) Stability measurements under N$_2$ environment (H$_2$O < 0.1 ppm) for $\chi = 0.2$ for both enantiomers.

wavelength that transfers from the cutoff filter in range of 400–700 nm. Figure 5a shows the measurement setup.

Table S1, Supporting Information presents the measured PV parameters, with CP, and without CP. It can be noticed from Table S1 and Figure S6, Supporting Information, that there is a significant decrease in the J_{SC} for all χ values when using CP, while the V_{OC} remains relatively similar. Basically, the decrease in the J_{SC} affects directly the efficiency of the device. One reason for that might be due to the relatively low transmittance ($\approx 40\%$ average visible transmittance (AVT)) of the polarizer, which influences directly the light intensity.[55] If we take the reduction in the transmittance into account, we can predict the final J_{SC} that can be observed using the polarizer. Figure 5b presents the ratio in percentage between the theoretical J_{sc} to the experimental J_{sc} for the different χ values. It can be seen that when we decrease the χ value, the mismatch between the theoretical J_{SC} and the experimental J_{SC} increases. For example, the degree of suitability for SCs with $\chi = 0.3$ is 93% while for $\chi = 0.15$ it is just 62%; for 3D, the most significant mismatch was found to be only 49%. These results indicate that even in the case of small amount of chiral barrier molecule (low χ value) there is an influence of the chiral barriers on the PV performance. Charge extraction (CE) analysis is presented in Figure 5c. This measurement can provide information about the transport, trapping, and back reaction of the charges in the SC. A typical charge extraction experiment is composed of four steps: i) a 2 s step in which the device is being discharged at the dark. ii) the device is being disconnected and illuminated for 2 s. iii) The light is switched off and the system waits for a certain time called delay time. In this step, a charge recombination occurs inside the device. Finally, the device is reconnected and the charges which were left and didn't recombine are extracted and measured. This process is being repeated for different delay times, from 0.5 to 15 s. The charges collected are plotted against the delay time to give insight on the lifetime of the charges after certain delay time. Figure 5c shows the behavior of typical devices, from $\chi = 0.3$ to 3D. It can be observed that the rate of recombination is the slowest for the 3D perovskite and it's being increased with the increase of the χ values. This indicates that in the case of $\chi = 0.3$, there are less charges left to extract after a certain delay time, therefore the recombination rate in this device structure is the highest. These measurements were performed on full devices; however, they are in a good agreement with the PL lifetime measurement (Figure 2c), which show the longest τ for the 3D perovskite as well. The external quantum efficiency (EQE) spectra are shown in Figure 5d. Clearly, when reducing the χ value, the EQE is reaching higher values. The J_{sc} integrated from the EQE spectra is in good agreement with the J_{sc} measured by the solar simulator for all cases (the deviation between the J_{sc} is less than 10% for all cases).

It is known that 2D and quasi-2D perovskite structures should enhance the stability of the perovskite.[22] In this work, we study the stability of the PSCs under two different environment conditions; under relatively high humidity (43–49%) (Figure 5e and S7a,c, Supporting Information) and under N_2 environment ($H_2O < 0.1$ ppm, $O_2 < 0.1$ ppm) (Figure 5f and S7b,d, Supporting Information). In both cases, the temperature was 18–25 °C. These stability measurements were performed for the S and R enantiomers. In the case of stability

test under relatively high humidity, the efficiency was preserved for 80 days for both enantiomers for the various χ values. Demonstrating the effect of the hydrophobicity of the barrier molecule. The cells were also stable for 8 months under N_2 environment (Figure 5f and S7b, Supporting Information); in this case, the 3D perovskite degraded slightly by 30% during the 8 months. In contrast, the R and S enantiomers were stable for the whole period of time.

3. Conclusions

This work presents the introduction of chiral molecules into 2D perovskite structure. Different χ values were synthesized (i.e., pure 2D, $\chi = 2$, 0.7, 0.4, 0.3, 0.2, 0.15, and 3D) for the two enantiomers. Using CD measurements, it was found that at high χ values, the chirality is more meaningful while at low χ values the chirality is less pronounced. Calculating the g_{abs} for the different χ values shows an increase by order of magnitude when the χ values were increased. SC-XRD reveals the exact configuration of the 2D perovskite chiral enantiomers. For the first time, these 2D chiral perovskites were introduced into SCs. We found a good correlation between the theoretical J_{sc} to the experimental J_{sc} at high χ values where this mismatch is increasing when the χ value decreased, which shows that even in the case of small amount of chiral barrier molecule (low χ value), the PV performance is affected.

4. Experimental Section

Device Fabrication: FTO conductive glass was etched by the reaction of zinc powder with HCl (37% Sigma). After etching, the glass was cleaned with 2.2 mL of Hellmanex III in 100 mL thermal dewatering (TDW) in a sonication bath for 10 min and then, was cleaned with isopropanol for 25 min in a sonication bath. Followed by oxygen plasma treatment (80% power, Diener). Then, a blocking layer of TiO_2 (lithium bis-(trifluoromethylsulfonyl)imide [99.95%, Sigma-Aldrich]) is created by spin-coating (5000 rpm, 30 s) the titanium diisopropoxide bis(acetylacetonate) diluted in absolute ethanol (200 μL in 1.5 mL). The substrates were annealed at 450 °C for half an hour in room environment. After cooling down, a mesoporous TiO_2 (Greatcell's product: 90T paste, diluted 1:6 in absolute ethanol) layer was coated on the substrates using the spin-coater (5000 rpm, 30 s), followed by annealing the substrates at 500 °C for 30 min in room environment. After going up to room temperature, these substrates were placed in aqueous $TiCl_4$ solution (1.6 mL in 140 mL TDW) (practical grade, FUJIFILM Wako Pure Chemical Corporation, Japan) and maintained at 70 °C for 30 min in the oven, followed by annealing the electrodes at 450 °C for another 30 min. These electrodes were stored in a nitrogen-filled glove box prior to completing the device fabrication.

When it was cooled down to 100 °C, the substrates were inserted to the glove box immediately. For the perovskite deposition, 45 μL of perovskite solution was dropped on the middle of the substrate, followed by a spin-coating process with a 5 s delay time, 10 s spin at 1000 rpm, and 45 s spin at 5000 rpm. Before 15 s the end of the spin coating, 100 μL of chlorobenzene was added dropwise onto the substrate. The cells were annealed at 100 °C for 45 min. After cooling down, solution of hole-transport material (Spiro-OMeTAD 54 mg in 750 μL chlorobenzene + 13.13 μL Li salt solution (52 mg lithium bis- (trifluoromethylsulfonyl)imide in 100 μL acetonitrile) + 21.6 μL TBP) was spin-coated (4500 rpm, 35 s). Finally, a 70 nm thick gold electrode was thermally evaporated on the film under a vacuum of $\approx 10^{-7}$ Torr.

Barriers Precursor Synthesis: Synthesis of (R)-(+)-α-Methylbenzylammonium iodide (R-MBA) and (S)-(-)-α-Methylbenzylammonium iodide (S-MBA) was

done dropwise: 2.5 mL of hydroionic acid (48 wt% in water, Aldrich) into a stirring solution of 2 mL R/S-MBA (amine) (99%, Aldrich) dissolved in 1 mL of ethanol absolute. After the addition of acid, the precipitate was left for 20 min at the same temperature. Following, reflux of 2 h in 120 °C. Then, the flask connects to rotor evaporator and the synthesis was at 80 °C until the liquid became very viscose. After cooling down to room temperature, adding 15 mL diethyl ether and stirring it until a white solid form can be discerned, the precipitate was washed with diethyl ether until its color became white, dried in oven for 12 h at 70 °C, and placed in glove box.

Preparation of Perovskite Solutions for Optical, Structural, and Morphological Analysis: The perovskite solutions were prepared in a nitrogen filled glove box $H_2O < 0.1$ ppm and $O_2 < 2.0$ ppm. All of the inorganic precursors were purchased from Sigma-Aldrich. The 2D and quasi-2D perovskite were prepared by dissolving stoichiometric quantity amounts of S-MBA or R-MBA salts, CsI, FAI, $PbBr_2$, and PbI_2 according to the molecular formula of $MAPbI_3 \cdot \chi(S/R\text{-}MBA)_2PbI_4$ where χ is calculated by the ratio the barrier molecules to the small cation (A^+) in the stoichiometric formula in dimethylformamide: dimethyl sulfoxide (DMF: DMSO_0.825:0.175).

Preparation of Perovskite Solutions for Devices: The perovskite solutions were prepared in a nitrogen-filled glove box $H_2O < 0.1$ ppm and $O_2 < 2.0$ ppm. All of the inorganic precursors were purchased from Sigma-Aldrich.

$Cs_{0.2}FA_{0.8}PbI_{2.75}Br_{0.25}$ (corresponds for $n = \infty$ (3D)) solution was prepared by dissolving CsI, FAI, $PbBr_2$, and PbI_2 in DMF:DMSO (DMF:DMSO_0.825:0.175) at 1.2 M concentration. The 2D and quasi-2D perovskite was prepared by dissolving stoichiometric quantity amounts of S-MBA or R-MBA salts, CsI, FAI, $PbBr_2$, and PbI_2 according to the molecular formula of $Cs_{0.2}FA_{0.8}PbI_{2.75}Br_{0.25}\cdot\chi(S/R\text{-}MBA)_2PbI_{2.75}Br_{0.25}$ (according to the exact χ value) in DMF:DMSO (DMF:DMSO_0.825:0.175).

Absorbance Measurements: Absorbance measurements were performed using a Jasco V-670 spectrophotometer.

PL Measurements: PL measurements and PL life time were measured by HORIBA FlouroMax 4, using light source of ozone-free xenon arc lamp 150-W. The sample PL was detected by a photon-counting detector (R928P photomultiplier tube), and a reference detector of UV-enhanced silicon photodiode. The samples were excited at a wavelength of 500 nm, slit size 5. PL life time was measured by 730 nm laser excitation or 350 nm laser excitation (depending on χ value).

Ultrahigh-Resolution SEM (UHR-SEM): Magellan XHRSEM was performed using a field-emission instruments (FEI), The Netherlands. The measurement conditions were 2 kV.

PV Characterization: Like mentioned before, we are using two optical components to cut off the light to exact wavelength after polarizing it. Therefore, the cutoff filter is BP550 Near-IR/UV-Block Visible Bandpass Filter (MIDOPT). Useful range: 405–690 nm, full width at half maximum (FWHM): 300 nm, tolerance: +/− 10 nm, peak transmission: ≥90%, surface quality: 40/20. The circular polarizer is PC052 Circular Polarizer (MIDOPT). Useful range: 400–700 nm, contrast ratio: 700:1, surface quality: 40/20, average transmission of 39% from 400 to 700 nm. (Figure S8, Supporting Information, presents the transmittance spectra of the cutoff filter and the circular polarizer).

PV measurements were performed using a Newport system, composed of an Oriel I–V test station using an Oriel Sol3A simulator. The solar simulator was class AAA for spectral performance, uniformity of irradiance, and temporal stability. The solar simulator was equipped with a 450 W xenon lamp. The output power was adjusted to match AM1. The spectrally matched classic cations were IEC60904-92 007, JIC C 8912, and ASTM E927-05.

The EQE was measured in 8 s with a fast EQE system from QUANTUM ZURICH (Switzerland). The SC was illuminated, with a spot of 4 mm in diameter, by 35 light-emitting diodes (LEDs), whose wavelengths lie in the range from 390 to 1080 nm. All the LEDs were simultaneously on and each one was driven at a different frequency, ranging from 55 to 555 Hz. During each measurement, a reference photodiode was used to measure the number of photons arriving on the SC. The system was calibrated with a reference National Institute of Standards and Technology (NIST)-traceable Si photodetector from Thorlabs. The total J_{sc} was calculated from the EQE data by using the spectral irradiance of AM1.5G spectrum at 1 sun solar intensity.

Charge Extraction: The measurements were performed using Autolab Potentiostat-Galvanostat (PGSTAT) with a FRA32M LED driver equipped with a white light source when the illumination was from the back (glass) side. The measurements were taken in Nova 1.1 software program to collect and analyze the data. The first step was identical to the voltage decay measurements. In the second step, the light was shut down and the system waited for certain time (delay time) before reconnecting and collecting the remained charges. The measurement had several cycles where in each cycle had a different delay time between 0.5 and 20 s.

Calculation Details: First, the DFT calculations were performed using the plane–wave QUANTUM ESPRESSO (QE) package.[56] The Perdew–Burke–Ernzerhof parametrization for the exchange–correlation functional was chosen. Norm-conserving pseudopotentials with the kinetic energy cutoff of 100 Ry for the wave functions were used. The first Brillouin zone was sampled with the $4 \times 4 \times 1$ Monkhorst-Pack grid. In the next step, the many-body effects within the non-self-consistent GW approximation (called G_0W_0)[57] were taken into account using YAMBO code.[58] The electronic screening was calculated within the plasmon–pole approximation.[59] The k–point grid of $2 \times 2 \times 1$ was used due to the large elementary cells and quite flat bands. The plane waves energy cutoff 20 Ry was used for the exchange self-energy. The dielectric matrix was constructed by summing 800 unoccupied bands and using the plane waves energy cutoff 6 Ry. Up to 600 unoccupied bands were included in the G_0W_0 summation. The BSE[60] has been solved for the active space of 12 and 14 occupied bands for the system S-MBA $n = 1$ and R-MBA $n = 1$, respectively, and 12 unoccupied bands for both cases. The exchange interactions were calculated with the plane waves energy cutoff 17 Ry and the Brillouin zone sampling was set to $4 \times 4 \times 4$. The CD, as implemented in the YAMBO code, was simulated within the noninteracting particles scheme using only the Γ-point for the BZ summation,[61] including the spin–orbit coupling (SOC).

Supporting Information

Supporting Information is available from the Wiley Online Library or from the author.

Acknowledgements

Conflict of Interest

The authors declare no conflict of interest.

Data Availability Statement

The data that support the findings of this study are available in the supplementary material of this article.

Keywords

[1] P. P. Boix, K. Nonomura, N. Mathews, S. G. Mhaisalkar, *Mater. Today* **2014**, *17*, 16.

[2] K. Wojciechowski, S. D. Stranks, A. Abate, G. Sadoughi, A. Sadhanala, N. Kopidakis, G. Rumbles, C.-Z. Li, R. H. Friend, A. K.-Y. Jen, H. J. Snaith, *ACS Nano* **2014**, *8*, 12701.

[3] T. Ishihara, *J. Lumin.* **1994**, *60–61*, 269.

[4] A. Shpatz Dayan, X. Zhong, M. Wierzbowska, C. E. M. De Oliveira, A. Kahn, L. Etgar, *Mater. Adv.* **2020**, *1*, 1920.

[5] J. Shamsi, A. S. Urban, M. Imran, L. De Trizio, L. Manna, *Chem. Rev.* **2019**, *119*, 3296.

[6] A. M. A. Leguy, P. Azarhoosh, M. I. Alonso, M. Campoy-Quiles, O. J. Weber, J. Yao, D. Bryant, M. T. Weller, J. Nelson, A. Walsh, M. Van Schilfgaarde, P. R. F. Barnes, *Nanoscale* **2016**, *8*, 6317.

[7] Q. A. Akkerman, V. D'Innocenzo, S. Accornero, A. Scarpellini, A. Petrozza, M. Prato, L. Manna, *J. Am. Chem. Soc.* **2015**, *137*, 10276.

[8] C.-W. Chen, S.-Y. Hsiao, C.-Y. Chen, H.-W. Kang, Z.-Y. Huang, H.-W. Lin, *J. Mater. Chem. A* **2015**, *3*, 9152.

[9] C. Li, X. Lu, W. Ding, L. Feng, Y. Gao, Z. Guo, *Acta Crystallogr. Sect. B Struct. Sci.* **2008**, *64*, 702.

[10] K. Pinsuwan, C. Boonthum, T. Supasai, S. Sahasithiwat, P. Kumnorkaew, P. Kanjanaboos, *J. Mater. Sci.* **2020**, *55*, 3484.

[11] M. Kumar, V. Pawar, P. A. Jha, S. K. Gupta, A. S. K. Sinha, P. K. Jha, P. Singh, *J. Mater. Sci. Mater. Electron.* **2019**, *30*, 6071.

[12] R. A. Belisle, W. H. Nguyen, A. R. Bowring, P. Calado, X. Li, S. J. C. Irvine, M. D. Mcgehee, P. R. F. Barnes, B. C. O'regan, *Energy Environ. Sci.* **2017**, *10*, 192.

[13] S. D. Stranks, G. E. Eperon, G. Grancini, C. Menelaou, M. J. P. Alcocer, T. Leijtens, L. M. Herz, A. Petrozza, H. J. Snaith, *Science* **2013**, *342*, 341.

[14] H.-S. Kim, I. Mora-Sero, V. Gonzalez-Pedro, F. Fabregat-Santiago, E. J. Juarez-Perez, N.-G. Park, J. Bisquert, *Nat. Commun.* **2013**, *4*, 2242.

[15] Best Research-Cell Efficiency Chart, NREL Photovoltaic Research, **2021**. https://www.nrel.gov/pv/assets/pdfs/best-research-cell-efficiencies.20191106.pdf (accessed: May 2021).

[16] B. Saparov, D. B. Mitzi, *Chem. Rev.* **2016**, *116*, 4558.

[17] L. Dou, A. B. Wong, Y. Yu, M. Lai, N. Kornienko, S. W. Eaton, A. Fu, C. G. Bischak, J. Ma, T. Ding, N. S. Ginsberg, L.-W. Wang, A. P. Alivisatos, P. Yang, *Science* **2015**, *349*, 1518.

[18] S. Ma, M. Cai, T. Cheng, X. Ding, X. Shi, A. Alsaedi, T. Hayat, Y. Ding, Z. Tan, S. Dai, *Sci. China Mater.* **2018**, *61*, 1257.

[19] J. Wang, J. Dong, F. Lu, C. Sun, Q. Zhang, N. Wang, *J. Mater. Chem. A* **2019**, *7*, 23563.

[20] D. B. Mitzi, *J. Solid State Chem.* **1999**, *145*, 694.

[21] D. B. Mitzi, C. A. Feild, W. T. A. Harrison, A. M. Guloy, *Nature* **1994**, *369*, 467.

[22] A. Shpatz Dayan, B.-E. Cohen, S. Aharon, C. Tenailleau, M. Wierzbowska, L. Etgar, *Chem. Mater.* **2018**, *30*, 8017.

[23] H. Tsai, W. Nie, J.-C. Blancon, C. C. Stoumpos, R. Asadpour, B. Harutyunyan, A. J. Neukirch, R. Verduzco, J. J. Crochet, S. Tretiak, L. Pedesseau, J. Even, M. A. Alam, G. Gupta, J. Lou, P. M. Ajayan, M. J. Bedzyk, M. G. Kanatzidis, A. D. Mohite, *Nature* **2016**, *536*, 312.

[24] Y. Liu, M. Siron, D. Lu, J. Yang, R. Dos Reis, F. Cui, M. Gao, M. Lai, J. Lin, Q. Kong, T. Lei, J. Kang, J. Jin, J. Ciston, P. Yang, *J. Am. Chem. Soc.* **2019**, *141*, 13028.

[25] B.-E. Cohen, Y. Li, Q. Meng, L. Etgar, *Nano Lett.* **2019**, *19*, 2588.

[26] Y. Li, J. V. Milić, A. Ummadisingu, J.-Y. Seo, J.-H. Im, H.-S. Kim, Y. Liu, M. I. Dar, S. M. Zakeeruddin, P. Wang, A. Hagfeldt, M. Grätzel, *Nano Lett.* **2019**, *19*, 150.

[27] D. Lu, G. Lv, Z. Xu, Y. Dong, X. Ji, Y. Liu, *J. Am. Chem. Soc.* **2020**, *142*, 11114.

[28] Z. Fang, X. Hou, Y. Zheng, Z. Yang, K.-C. Chou, G. Shao, M. Shang, W. Yang, T. Wu, *Adv. Funct. Mater.* **2021**, *31*, 2102330.

[29] Y.-W. Jang, S. Lee, K. M. Yeom, K. Jeong, K. Choi, M. Choi, J. H. Noh, *Nat. Energy* **2021**, *6*, 63.

[30] X. Li, et al., *Adv. Energy Mater.* **2020**, *10*.

[31] R. Naaman, D. H. Waldeck, *J. Phys. Chem. Lett.* **2012**, *3*, 2178.

[32] R. Naaman, D. H. Waldeck, *Ann. Rev. Phys. Chem.* **2015**, *66*, 263.

[33] Y. Wu, J.-C. Xu, *Tetrahedron* **2001**, *57*, 8107.

[34] X. Liu, S. Dong, L. Lin, X. Feng, *Chinese J. Chem.* **2018**, *36*, 791.

[35] A. Ishii, T. Miyasaka, *Sci. Adv.* **2020**, *6*, 3274.

[36] Y.-H. Kim, Y. Zhai, H. Lu, X. Pan, C. Xiao, E. A. Gaulding, S. P. Harvey, J. J. Berry, Z. V. Vardeny, J. M. Luther, M. C. Beard, *Science* **2021**, *371*, 1129.

[37] H. Duim, M. A. Loi, *Matter* **2021**, *4*, 3835.

[38] M. P. Moloney, Y. K. Gun'ko, J. M. Kelly, *Chem. Commun.* **2007**, 3900, https://doi.org/10.1039/b704636g.

[39] D. G. Billing, A. Lemmerer, *CrystEngComm*, **2006**, *8*, 686.

[40] Y. Dang, X. Liu, Y. Sun, J. Song, W. Hu, X. Tao, *J. Phys. Chem. Lett.* **2020**, *11*, 1689.

[41] J. Ahn, S. Ma, J.-Y. Kim, J. Kyhm, W. Yang, J. A. Lim, N. A. Kotov, J. Moon, *J. Am. Chem. Soc.* **2020**, *142*, 4206.

[42] J. Ma, C. Fang, C. Chen, L. Jin, J. Wang, S. Wang, J. Tang, D. Li, *ACS Nano* **2019**, *13*, 3659.

[43] H. Lu, C. Xiao, R. Song, T. Li, A. E. Maughan, A. Levin, R. Brunecky, J. J. Berry, D. B. Mitzi, V. Blum, M. C. Beard, *J. Am. Chem. Soc.* **2020**, *142*, 13030.

[44] H. Lu, J. Wang, C. Xiao, X. Pan, X. Chen, R. Brunecky, J. J. Berry, K. Zhu, M. C. Beard, Z. V. Vardeny, *Sci. Adv.* **2019**, *5*, eaay0571.

[45] D. Di Nuzzo, L. Cui, J. L. Greenfield, B. Zhao, R. H. Friend, S. C. J. Meskers, *ACS Nano* **2020**, *14*, 7610.

[46] J. Ahn, E. Lee, J. Tan, W. Yang, B. Kim, J. Moon, *Mater. Horiz.* **2017**, *4*, 851.

[47] H. Kim, Y.-J. Jin, B. S.-I. Kim, T. Aoki, G. Kwak, *Macromolecules* **2015**, *48*, 4754.

[48] B. Cai, X. Li, Y. Gu, M. Harb, J. Li, M. Xie, F. Cao, J. Song, S. Zhang, L. Cavallo, H. Zeng, *Sci. China Mater.* **2017**, *60*, 811.

[49] J. Even, L. Pedesseau, C. Katan, *ChemPhysChem* **2014**, *15*, 3733.

[50] Economics Principles and Applications - Google Books.

[51] J. A. Schellman, P. Oriel, *J. Chem. Phys.* **1962**, *37*, 2114.

[52] N. Berova, K. Nakanishi, R. W. Woody, *Circular Dichroism: Principles and Applications*, 2nd ed., **2000**, p. 912.

[53] A. Ben-Moshe, A. Teitelboim, D. Oron, G. Markovich, *Nano Lett.* **2016**, *16*, 7467.

[54] P. L. Polavarapu, *J. Phys. Chem. A* **2005**, *109*, 7013.

[55] I. A. Yunaz, et al. in *Conf. Record of the IEEE Photovoltaic Specialists Conf.*, **2009**, pp. 000153–000157, https://doi.org/10.1109/pvsc.2009.5411706.

[56] P. Giannozzi, S. Baroni, N. Bonini, M. Calandra, R. Car, C. Cavazzoni, D. Ceresoli, G. L. Chiarotti, M. Cococcioni, I. Dabo, A. Dal Corso, S. De Gironcoli, S. Fabris, G. Fratesi, R. Gebauer, U. Gerstmann, C. Gougoussis, A. Kokalj, M. Lazzeri, L. Martin-Samos, N. Marzari, F. Mauri, R. Mazzarello, S. Paolini, A. Pasquarello, L. Paulatto, C. Sbraccia, S. Scandolo, G. Sclauzero, A. P. Seitsonen, A. Smogunov, et al., *J. Phys. Condens. Matter* **2009**, *21*, 395502.

[57] L. Hedin, *Phys. Rev.* **1965**, *139*, A796.

[58] D. Sangalli, A. Ferretti, H. Miranda, C. Attaccalite, I. Marri, E. Cannuccia, P. Melo, M. Marsili, F. Paleari, A. Marrazzo, G. Prandini, P. Bonfà, M. O. Atambo, F. Affinito, M. Palummo, A. Molina-Sánchez, C. Hogan, M. Grüning, D. Varsano, A. Marini, *J. Phys. Condens. Matter* **2019**, *31*, 325902.

[59] A. Urushibara, Y. Moritomo, T. Arima, A. Asamitsu, G. Kido, Y. Tokura, *Phys. Rev. B* **1995**, *51*, 14103.

[60] E. E. Salpeter, H. A. Bethe, *Phys. Rev.* **1951**, *84*, 1232.

[61] D. Varsano, L. A. Espinosa-Leal, X. Andrade, M. A. L. Marques, R. Di Felice, A. Rubio, *Phys. Chem. Chem. Phys.* **2009**, *11*, 4481.